Shielded radiography with a laser-driven MeV-energy x-ray source

Shouyuan Chen, Grigory Golovin, Daniel Haden, Sudeep Banerjee, Ping Zhang, Cheng Liu, Jun Zhang, Baozhen Zhao, and Donald Umstadter*

Department of Physics and Astronomy, University of Nebraska-Lincoln, Lincoln, Nebraska 68508, USA

Cameron Miller, Shaun Clarke, and Sara Pozzi

Department of Nuclear Engineering and Radiological Sciences, University of Michigan, Ann Arbor, Michigan 48109, USA

*Corresponding author: donald.umstadter@unl.edu

Abstract:

We report the results of experimental and numerical-simulation studies of shielded radiography using narrowband MeV-energy x-rays from a compact all-laser-driven inverse-Compton-scattering x-ray light source. This recently developed x-ray light source is based on a laser-wakefield accelerator with an ultra-high-field gradient (GeV/cm). We demonstrate experimentally high-quality radiographic imaging (image contrast of 0.4 and signal-to-noise ratio of 2:1) of a target composed of 8-mm thick depleted uranium shielded by 80-mm thick steel, using a 6 MeV x-ray beam with a spread of 45% (FWHM) and 10^7 photons in a single shot. The corresponding dose of the x-ray pulse to obtain such radiography is measured in front of the target, which is ~100 nGy/pulse. Simulations performed using the Monte-Carlo code MCNPX accurately reproduce the experimental results. Moreover, these simulations also demonstrate that the narrow bandwidth of the Compton x-ray source operating at 6 and 9 MeV leads to a reduction of deposited dose as compared to broadband bremsstrahlung sources with the same end-point energy. The x-ray beam's inherently low-divergence angle (~mrad) is advantageous and effective for interrogation at standoff distance. These results demonstrate several significant benefits of all-laser driven Compton x-rays for shielded radiography.

Key words: Radiography, laser, wakefield, inverse Compton, Thomson scattering, x-ray, Monte Carlo simulation, cargo inspection, monoenergetic.

1. Introduction

Nuclear materials smuggling is considered to be a serious global security threat [1]. Given the large number of cargo containers (over 100 million) that are transported around the world each year [2], they have long been considered as a possible vehicle for illegal transport of nuclear weapons and special nuclear materials (SNM). To mitigate this potential threat, it is critical to detect these illicit materials early, while they are in transport or upon their arrival at seaports. Many detection technologies are currently in use at seaports worldwide to detect SNM [3]. Passive technologies are a common method for SNM detection, and function by detecting radiation signatures emitted by SNM. However, certain SNM, such as highly enriched uranium, can be easily shielded to defeat passive detection [4]. Active interrogation technologies provide an alternative solution by detecting SNM based on other signatures of SNM materials, such as density and atomic number. Among the active interrogation technologies, including x-ray, neutron or muon radiography [5-7], x-ray radiography is the most mature technology for the detection of dense shielded materials. The requirements for safe and accurate inspections that can be performed on cargo-container inspections is subject to multiple constraints and this limits the choice of parameters for the x-ray bean. For instance, to achieve sufficient penetration depth through thick shielding, a photon energy of ~6 MeV is required [3, 8]. Maintaining a safe level of radiological dosage to both the target and bystanders requires a relatively narrow x-ray bandwidth [9, 10]. Material discrimination by means of the *Z*-scanning technique requires tunability of the x-ray photon energy. This technique exploits the fact that different materials have different energy dependence for the attenuation coefficient which enables them to be distinguished using dual or multi-energy radiography [11, 12]. A highly collimated x-ray beam is required in a scenario where standoff interrogation is the only possibility [13]. Currently, there is significant effort expended to develop a single x-ray source that can simultaneously meet all of these requirements.

Inverse-Compton-scattering (ICS) sources produce narrowband, and tunable multi-MeV x-ray beams with small beam angular spread and can simultaneously meet all of the above requirements. While the most commonly used x-ray source, based on bremsstrahlung radiation, produces the requisite energy, it has a continuous spectrum and significant divergence. Standard radioisotope sources produce narrow bandwidth x-rays [9], but their x-ray energies are restricted to ≤ 1.5 MeV and they cannot be tuned. However, the application of ICS sources based on conventional electron accelerators is limited by their size [14, 15]. The recently developed laser-wakefield-accelerator-driven inverse-Compton-scattering (LWFA-ICS) source overcomes this limitation by using a 1,000 times higher acceleration gradient of a plasma wakefield compared with conventional RF technology, and provides a compact x-ray source with well-collimated (mrad), narrowband ($\Delta E/E \sim 0.5$), and tunable (from 1 to 9 MeV) beams [16-19].

In this paper, we experimentally demonstrate radiography of a shielded uranium target with a LWFA-ICS source [16-19]. Using numerical simulationand experimental results, we show that LWFA-ICS source is an exciting new device for the radiography of cargo containers and can potentially transform this area.

2. Radiography experiment

In the following, we report the results of the experimental proof-of-principle study of x-ray radiography with a LWFA-ICS source [16-18]. We also present the results of MCNPX simulations that show that our current x-ray parameters meet the requirements for x-ray radiography of shielded cargo containers, in terms of required photon flux, energy spread, radiological dosage, and image quality.

2.1 Electron and x-ray beam generation and characterization

To demonstrate the image quality and quantify the dose of the laser driven x-ray source, we conducted radiography experiments using the 200-TW peak-power DIOCLES laser system housed in the Extreme Light Laboratory at the University of Nebraska-Lincoln. Fig. 1 shows the experimental setup used to generate high-energy x-rays. The uncompressed 7-J laser beam was split using a 70% / 30% beam splitter, with 4.9-J laser pulse transmitted and 2.1-J reflected. The reflected and transmitted beams were then directed into two independent compressors, and compressed to 35 fs, to be used as the drive and scattering beams, respectively. The drive laser pulse, with 3-J energy after the compressor, was focused by a 1-m off-axis parabola to a 20-μm (FWHM) focal spot, with 40% energy enclosed in the FWHM contour. The focus was located on the rising edge of a 6-mm-long supersonic gas target (99% helium and 1% nitrogen) at a height of 1.5 mm above the nozzle. The electron beam spectra were then measured with a magnetic spectrometer, consisting of a 5.5-in round magnet (0.7 T) and a 6-inch rectangular magnet (0.7 T), and a fluorescent screen (LANEX) imaged by a 12-bit CCD camera. Due to the limits of LANEX size, the spectrometer has an energy cutoff at 150 MeV.

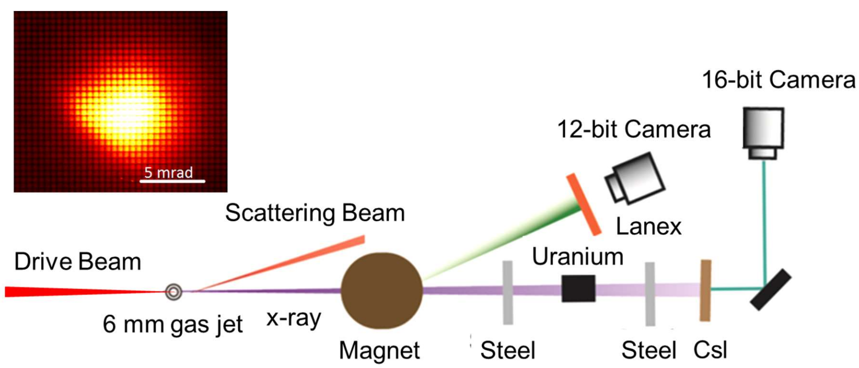

Fig. 1. Experimental setup for radiography experiment. The inset on the left corner shows the x-ray beam profile taken by the CsI detector, which has a divergence of 7 mrad (FWHM).

Fig. 2 (a) shows the typical spectrum of the measured electron beams. The electron beams had a charge of 50 pC, an angular divergence of ~5 mrad, and an energy spectrum that peaked at 500 MeV and extended to 600 MeV. A deconvolution process was applied to deconvolve the divergence of the electron beam from the measured electron beam deflection by the magnet spectrometer to obtain electron energy spectrum. Though LWFA accelerators with lower energy spread was demonstrated by separating the injection and acceleration stage, we chose 6 mm single nozzle with ionization injection in this experiment to provide the high charge and high energy electron to generated ~6 MeV x-ray beam. The generated x-ray beam profile was first measured by a calibrated 50-mm by 50-mm voxelated CsI detector with 1-cm thickness coupled to a 14-bit EM gain camera positioned before the radiography target. The x-ray beam had a divergence of ~7 mrad and ~10^7 photon number. The small divergence of the beam delivers the “pencil beam,” which is one of several beam types used in radiography. Fig. 3 (b) shows the calculated on-axis x-ray spectral intensity based on the electron spectrum, which is peaked at 6.5 MeV and extends up to 10 MeV with ~45% FWHM energy spread.

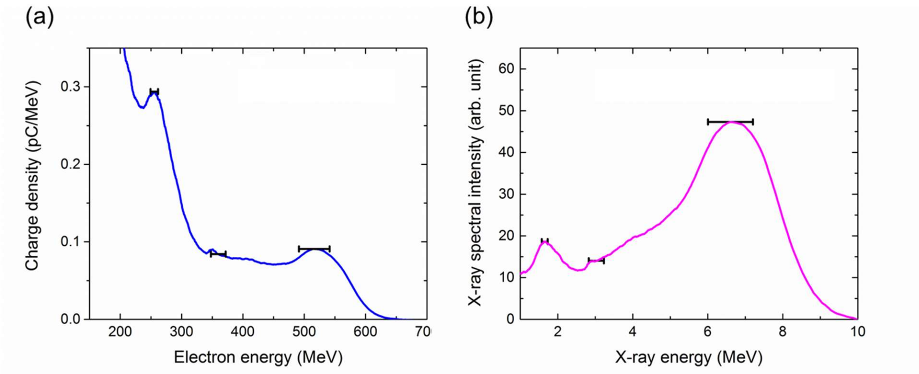

Fig. 2. Measured electron and x-ray energy spectra. a) Electron energy spectrum with a high energy peak at 520 MeV and low energy tail. The error bars represent the standard deviation of the electron beam energy due to the electron beam pointing stability into the magnet spectrometer at three electron beam energies. b) X-ray spectral intensity calculated based on the electron energy spectrum. The peaked x-ray spectrum is due to the fact that the spectral intensity is weighted by the x-ray energy. The error bars at the three x-ray energy points represent the uncertainty of x-ray energies at these points due to the error in electron beam energy measurement.

2.2 Radiography of shielded depleted uranium target

Subsequent to the characterization of the x-ray beam, we proceeded by obtaining radiographs using DIOCLES (MeV photon source). The radiography targets consisted of two layers of steel shielding (thicknesses varied from 6 mm to 40 mm) and uranium disks with 20-mm diameter and 6-8 mm thicknesses, as show in Fig. 3. The targets were positioned 3 m from the x-ray source. The radiography images were obtained by a 50-mm by 50-mm voxelated CsI with 2-cm thickness coupled to a 16-bit EMCCD camera operated in high-gain mode.

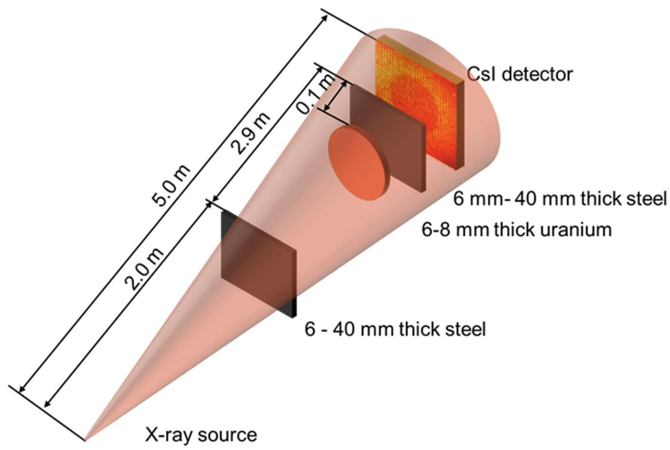

Fig. 3. Experimental setup used for radiography measurements a) Layout of the shielded uranium with respect to the source and detector. b) Side view of the geometry of the shielded uranium target.

Two important parameters to evaluate the quality of the radiography image are the image contrast and signal to noise ratio (SNR). The absolute contrast is defined as the change in intensity caused by the structure of interest [20]. In other words, it is the change of intensity caused by the structure of interest compared with the surrounding material. A more useful definition is relative contrast C, which is defined as:

$$C = \frac{\Delta I}{I}, \qquad (1)$$

where I is the average background intensity (in the vicinity of the structure of interest), and ΔI is the change in the intensity caused by the structure of interest. The SNR is defined as

$$SNR = \frac{\Delta I}{\sigma_I} = C\frac{I}{\sigma_I}, \qquad (2)$$

where σ_I is the standard deviation of the background intensity.

In the experiment, we first took a radiograph image of a 6-mm thick uranium disk without shielding, as shown in Fig. 4(a). We analyzed the average intensity in two areas: the adjacent area of the background and uranium disk covered by an area of 3 by 3 voxels, which have counts of ~9500 and ~4500, respectively. The standard deviation of the background intensity is ~900. Based on the contrast and SNR definition, the contrast of the image contrast is 0.46 and the SNR is ~4. We then took a radiograph of the 6-mm uranium disk shielded by 0.25-inch thick steel, both at the back and front, as shown in Fig. 4(b). Using the same procedure for unshielded uranium, we analyzed the image SNR of the shielded uranium target with the image intensity in the uranium target area and adjacent area. The intensity in the target area is 4250 counts and the adjacent area is 6480 counts. The standard deviation of the background intensity is about ~650 counts. The contrast of the image is ~ 0.39 and the SNR is ~3.

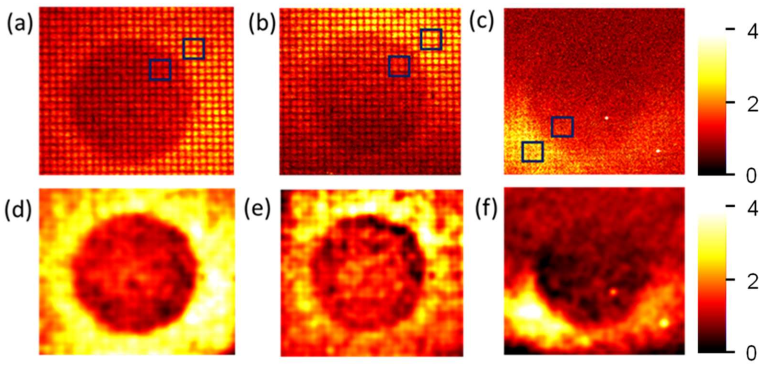

Fig. 4. Raw and processed radiography images of shielded uranium. (a) Radiography image of the 6-mm uranium disk without shielding. (b) Radiography image of the 6-mm uranium disk shielded by 0.25-in steel in back and front. (c) Radiography image of 8-mm uranium shielded by 1.5-inch steel. The area covering 3 by 3 voxels (indicated by the boxes in these images) was used to analyze the image quality. Images (d), (e), and (f) are the processed radiography images using a Fourier filter, which enhance the uranium disk image by removing the x-ray beam profile and grid of the CsI detector. It demonstrated that a more uniform radiography image can be obtained with post-processing to help distinguish the target.

We further tested the radiography imaging system with 8-mm uranium shielded by 1.5-inch steel in the front and back of the target. The radiography image is shown in Fig. 4(c). We performed the same image quality analysis and used the 3 by 3 voxel area in the target and adjacent area to obtain the contrast and SNR. The average intensity in the target area is 1750 counts and intensity in the adjacent area is 2960 counts with standard deviation of ~600 counts. This gives a contrast of ~0.41 and SNR of ~2. These images were also processed with a Fourier filter to remove the print of the x-ray beam intensity profile and the grid on the CsI detector. As shown in the Fig. 4 (d), (e) and (f), post-processing enhances the radiography image and makes it easier to distinguish the object.

From this study, it is interesting to note that the image contrast of radiography using the Thomson source was affected little by the increase in shielding thickness. The shielding mainly affected the SNR since the signal level drops with more shielding. Even with total shielding of 3-inch steel, we were able to obtain an image with SNR of 6 using the current detection system with a single x-ray pulse. Using a more sensitive detection system, such as $CdWO_4$ coupled to a PMT sensor, and multiple shots, we believe the SNR would be further improved.

Another important parameter for cargo container scanning is the dosage of the x-ray beam. The x-ray dose is measured using the ion chamber dosimeter (Radcal model 10x6-1800), which has a sensitivity of 0.01 nGy. The measured single shot x-ray dose in front of the radiography target is about 100 nGy. It is consistent with the calculated dose based on the x-ray energy spectrum and the 10^7 photon number measured by the calibrated CsI detector. Simulations discussed in a later section show that the narrowband x-ray beam can reduce the dose on the target by a factor of two. As the result, the narrowband x-ray source can better meet the dose requirements for x-rays used in cargo scanning: As Low as Reasonably Achievable (ALARA) [21].

The experimental results are compared with MCNPX simulation, using the same target geometry and x-ray spectrum shown in Fig. 5. The simulated image contrast is 0.40 for 0.25-inch steel shielded 6-mm thick uranium, and it is consistent with the experiment results of 0.39. For the case of 1.5-inch steel shielded 8-mm thick uranium, the simulated image contrast is 0.42, which also reasonably agrees with the measured value of 0.41.

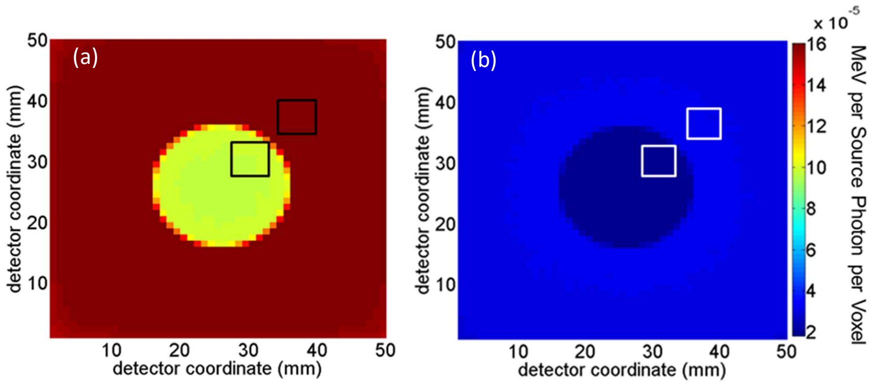

Fig. 5. MCNP simulation of the shielded uranium radiography. The image contrast is calculated with 9 voxels (indicated in the boxed areas). (a) The simulated radiography of the 6-mm shielded uranium, which has an image contrast of 0.40. (b) The simulated radiography of 8-mm shielded uranium, which has an image contrast of 0.42.

3. MCNP simulation of the narrowband x-ray radiography

Although the x-rays produced by LWFA-ICS sources have relatively low energy spreads ($\Delta E/E$ ~40%) compared with bremsstrahlung sources, their spreads are relatively large compared with the gamma rays generated from naturally occurring radioactive isotopes. It is therefore reasonable to ask how the radiographic image contrast and dose depend on x-ray energy spread. In this section, we use MCNPX simulations to address these questions and systematically study the advantages of the narrowband x-ray beam for cargo container radiography. This includes a comparison of narrowband x-ray beams and bremsstrahlung sources for radiography of shielded uranium in terms of dosage, and show that x-ray bandwidth up to 40% does not affect the image contrast.

3.1 Effect of x-ray bandwidth on radiography image.

To confirm the conclusion stated previously that up to 40% bandwidth of the x-ray beam at 6 MeV has little effect on radiography, we studied the image contrast of a narrowband x-ray source with different energy spreads. The simulation geometry is shown in Fig. 6. A 6-mm glass window in between the x-ray source and wood pallet is taken into account because the window is needed to keep the x-ray source in vacuum. The wood pallet has dimensions 107 cm by 107 cm by 101 cm; a 5-cm length HEU cube is located in the center. A 1.5-cm thick $CdWO_4$ detector is used in the simulation since it is a common detector for cargo container radiography. We also added the space between the x-ray source, pallet, and detector to account for the effect of air in this space. Fig. 7 shows the mid-plane lineout of deposited energy per photon source with x-ray beams with different central energy and bandwidth. By comparing these two cases, we found that the image contrast of radiography taken with 40% energy spread is nearly the same as that taken with 10% energy spread x-ray beam. X-ray beams with 40% energy spread have about 1% greater transmission ratio. This showed that the currently achieved energy spread of the Compton x-ray source is sufficient to provide the advantages of monoenergetic x-ray radiography.

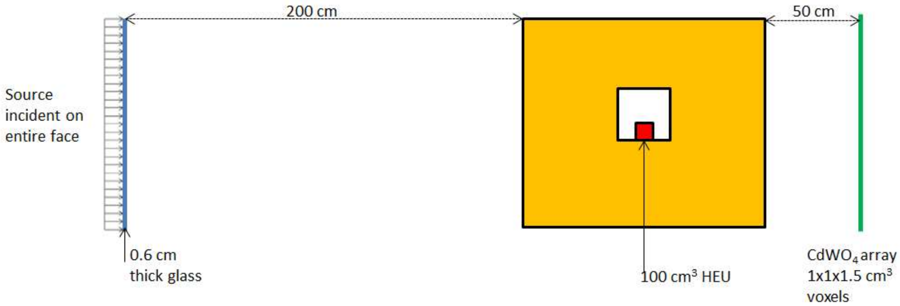

Fig. 6. Simulation setup of the wood pallet when the x-ray beam goes through a glass window and with system filled with air.

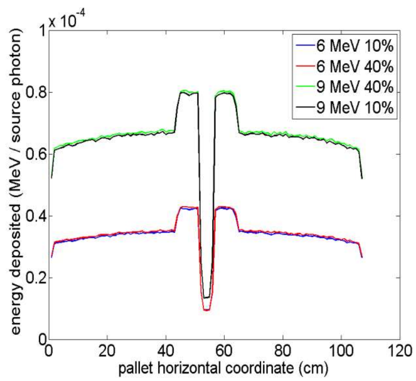

Fig. 7. Mid-plane cross sections of the radiography for two different examples.

This simulation also showed the required x-ray flux for radiography. Though the required x-ray source flux for cargo container scanning depends on various parameters, such as materials inside the cargo container, scan speed, detector sensitivity, and scan distance, the wood pallet can be taken as typical cargo composition. By adopting the criteria that a photon energy equal to 10 MeV needs to be deposited on a 1 cm^2 detector to form a radiography image, as was used in a prior study [22], as well as the fact that the energy deposited on the detector is a factor of 10^{-4} of the source photon energy for the wood pallet, we found that 10^5 photon/cm^2 is required to form a radiographic image with a narrow bandwidth x-ray source. Assuming a cargo container with height of 2 m, and

Commented [A1]: Needs correcting

Commented [A2R1]: Revised

a required scan speed of 10-100 cm s^{-1}, a photon flux of 10^8~10^9 photons per second is needed for the radiography. The maximum scan rate will be limited by the level of attenuation the x-ray beam experiences due to the objects in the cargo container.

3.2 On target dose reduction

Another interesting question for narrow bandwidth radiography is the on-target dose compared with a bremsstrahlung source. A bremsstrahlung source has a larger portion of lower energy photons (< 1 MeV), which results in a much larger fraction of absorption and scattering by the target. This leads to higher dose deposition on target. Using the same pallet setup as shown in Figure 6, we quantitatively evaluated the dose deposited on the target with different x-ray sources. To obtain and compare the absolute dose, we used the energy deposited on the detector as the criteria. In another words, the on-target doses are compared with the same image intensity obtained on the detector for different x-ray sources.

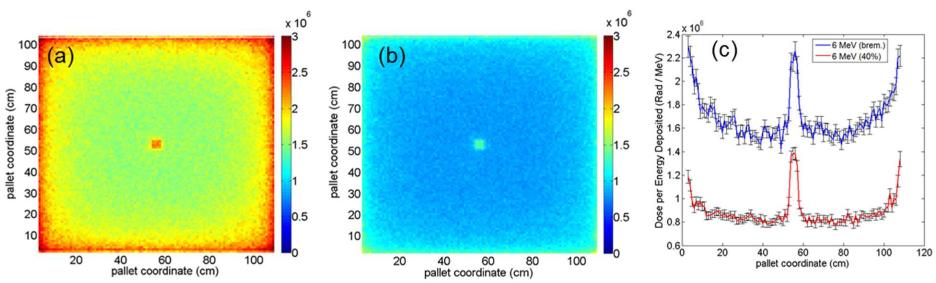

Fig. 8. MCNP simulation of on target dose comparison for 6 MeV narrowband x-ray source and bremsstrahlung source. a) Dose map of 6 MeV narrowband source with rad per MeV photon energy deposited on the detector. b) Dose map of 6 MeV bremsstrahlung source with rad per MeV photon energy deposited on the detector. c) Mid-plane cross sections of the dose map for two different 6 MeV sources. The error bars represent the standard deviation of the numerical simulation.

The dose comparison in Fig. 8 shows that a narrowband source at 6 MeV with 40% energy spread deposited two times less dose on target than that of a bremsstrahlung source with the same end point energy. In addition, we compared the deposited dose on the target between the 9 MeV narrowband x-ray source and the bremsstrahlung source with 9 MeV endpoint energy, and this also showed a dose reduction by a factor of two with the narrowband x-ray source. Using the same criteria, we studied the bystander dose at 1 meter away from the edge of the pallet. Additionally, we found the narrowband x-ray beam reduced the bystander dose by a factor of 10 as compared with the bremsstrahlung source at the same end-point energy. This finding of lower dose with narrowband x-rays has the potential to enable radiography systems that better comply with federal regulations limiting allowable dose to As Low As Reasonably Achievable (ALARA) [21].

3.3 Standoff propagation

The highly collimated inverse Compton x-ray beam is also advantageous for standoff interrogation. If we assume that a bremsstrahlung source has a photon number of 10^{14}/s (which is typical for those used for cargo container screening) distributed in a 60 degree half cone angle, the corresponding photon flux is 3.2×10^{13}/s/sr. For LWFA-ICS with 10 Hz operation rate, 4 mrad divergence angle, and 10^7 photon/shot, the photon flux is 8×10^{12}/s/sr. Taking into account the narrow bandwidth, the LWFA-ICS should have comparable or even higher photon flux/bandwidth at MeV range compared with the bremsstrahlung source. By increasing the current inverse Compton source repetition rate, such as using a 50-Hz diode pumped laser system, and operating LWFA in the polyenergetic regime to increase electron beam charge to nC, the LWFA-ICS flux can be further increased by one or two orders magnitude [23-25].

We simulated the long-standoff propagation of an x-ray beam with central energy of 9 MeV, energy spread of 10% FWHM, and 1×10^7 photons per pulse at 10 Hz. The divergence of the photon beam is analyzed by simulating its propagation over a 100-m long cylindrical column of air, with a 3-m radius. The beam is simulated as a cone with an opening angle of 2 mrad, which corresponds to the measured x-ray half cone angle at 9 MeV. Fig. 9 shows the spread of the beam at 100 m from the source. The results show that the beam is still concentrated in a 20-cm radius from the center of the beam. The x-ray attenuation due to air in this distance is 18.5%, Fig. 10 showed the evolution of the x-ray beam spectrum as a function of distance at 50 meter and 100 meter.

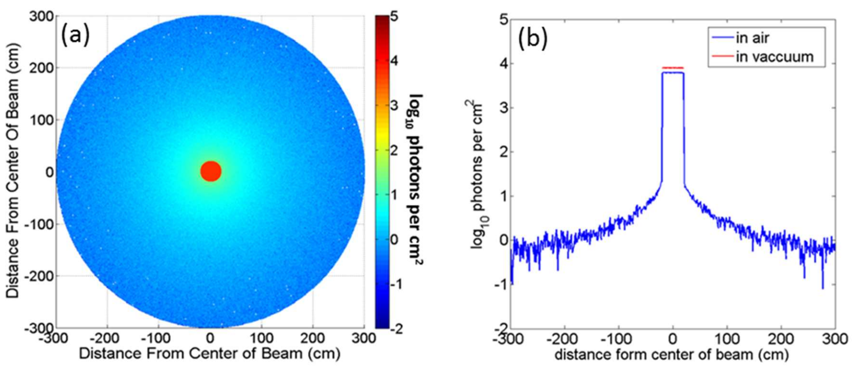

Fig. 9**.** MCNP simulation of 100 meter x-ray propagation in air. a) Photon flux map 100 m from source, per pulse. The red circle shows the x-ray beam size if it propagates in vacuum without scattering. b) Lineout of the photon distribution along the photon flux map center. The red line showed flux of photon if the x-ray beam propagates in vacuum without attenuation.

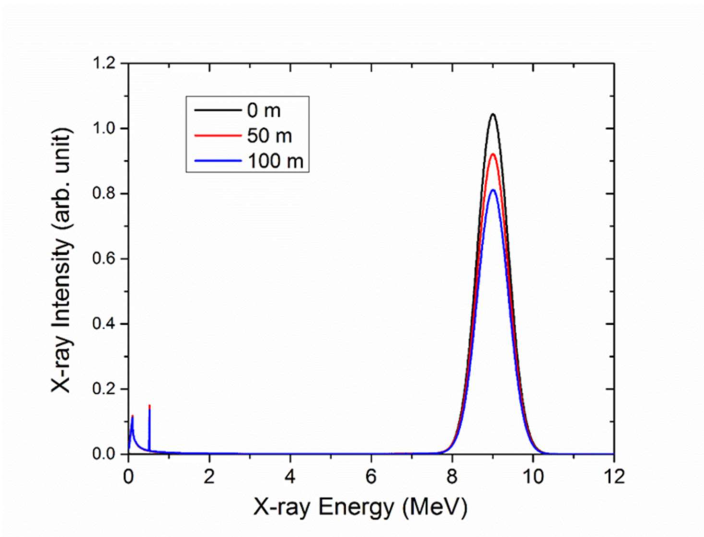

Fig. 10. The spectrum evaluation of the 9 MeV x-ray beam with 10% energy spread propagation in air. The black line show the original x-ray spectrum. The red and blue line show the x-ray spectrum after 50 m and 100 m propagation respectively.

The dose is also of interest at different points along the beam line. Fig. 11 shows doses measured at 10-m increments along the beam simulated by the MCNPX code.

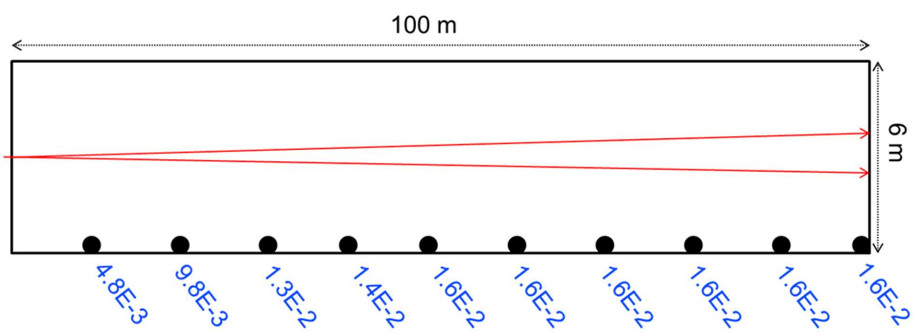

Fig. 11. Dose rates (mrem/hr) at distance of 3-m off-axis from the photon beam line.

From the simulation results, the scattering of the gamma ray beam is 18.5% for 100-m propagation without significant change on the spectrum shape, and the bystander dose is much less than the NRC limit of 5 mrem/hr. These results demonstrate that the inverse Compton source with narrow beam divergence is suitable for standoff interrogation.

4. Summary

Using both experiments and simulations, we studied the performances of various x-ray sources for shielded cargo radiography. The MCNP simulations showed that an energy spread as large as 40% results in significant dose reduction. Such narrow bandwidth has already been demonstrated experimentally by an LWFA-ICS x-ray source at the University of Nebraska-Lincoln [26]. We also experimentally demonstrated the capability of this LWFA-ICS source to obtain a single-shot radiograph of an 8-mm thick uranium disk, shielded with 76-mm steel, with an image contrast of 0.4, and SNR of 2. In terms of the on-target dose, the simulation study showed that narrowband x-ray beams are superior to bremsstrahlung x-rays with the same end-point energy. When comparable radiographic image quality is used as the comparison criteria, we find that the dose is not reduced by the large amount expected from previous studies [9, 26]. The reason is that there is a relatively flat x-ray attenuation curve in the MeV range, and therefore a large portion of x-ray photons from the 6-9 MeV bremsstrahlung source contributes to the radiographic image. We also found that other features of LWFA-ICS x-rays, such as the small divergence, makes the source suitable for both standoff interrogation and scanning in pencil-beam mode. In addition, the narrow bandwidth and high energy of the LWFA-ICS x-ray source permits the improvement of material discrimination through dual energy radiography [27-30], as well as implementation of sensitive threat alarms for isotope specific detection. While the x-ray system reported here occupies 2000 ft^2 (inclusive of both the laser system and the inverse-Compton source), its size can be reduced for applications. In fact, an inverse-Compton x-ray source can be built with currently available components to fit in the 400-ft^2 area of a flatbed truck. Given these many advantages, LWFA-ICS x-ray sources are potentially transformative for shielded radiography.

Acknowledgements

We thank K. Brown, J. Mills, and C. Petersen for their contributions to the laser facility, and thank N. Glasco for proofreading the manuscript. This material is based on work supported by the US Department of Energy (DOE), Office of Science, Basic Energy Sciences (BES), under Award # DE-FG02-05ER15663 (ultrafast x-ray science); the Air Force Office for Scientific Research, FA9550-11-1-0157 (high-field laser-electron scattering); the Department of Homeland Security Domestic Nuclear Detection Office, under competitively awarded contract HSHQDC-13-C-B0036 (low-dose x-ray radiography); and National Strategic Research Institute, FA4600-12-D-9000 (selective photo-activation analysis). This support does not constitute an express or implied endorsement on the part of the Government.

References

[1] G. Allison, *Nuclear Terrorism Fact Sheet*, Belfer Center for Science and International Affairs, Harvard Kennedy School. Belfer Center for Science and International Affairs. (April 2010.).

[2] *Container Security Initiative in Summary*, U.S. Customs and Border Protection. U.S. Department of Homeland Security (May 2011).

[3] Jonathan Medalia, *Detection of Nuclear Weapons and Materials: Science, Technologies, Observations*, CRS Report for Congress (2010), pp. R40154.

[4] G.M. Gaukler, C. Li, R. Cannaday, S.S. Chirayath and Y. Ding, *Detecting Nuclear Materials Smuggling: Using Radiography to Improve Container Inspection Policies*, Annals of Operations Research. 187 (2011), pp. 65-87.

[5] D. Slaughter, M. Accatino, A. Bernstein, J. Candy, A. Dougan, J. Hall, A. Loshak, D. Manatt, A. Meyer and B. Pohl, *Detection of Special Nuclear Material in Cargo Containers using Neutron Interrogation*, Lawrence Livermore National Laboratory, 2003.

[6] P. Baesso, D. Cussans, C. Thomay and J. Velthuis, *Toward a RPC-Based Muon Tomography System for Cargo Containers*, Journal of Instrumentation. 9 (2014), pp. C10041.

[7] G. Chen, *Understanding X-Ray Cargo Imaging*, Nuclear Instruments and Methods in Physics Research Section B: Beam Interactions with Materials and Atoms. 241 (2005), pp. 810-815.

[8] P. Bjorkholm, *Cargo Screening: Selection of Modality*, Port Technology International. 17 (2003), pp. 37-39.

[9] Victor Orphan, Ernie Muenchau, Jerry Gormley and Rex Richardson, *Advanced Cargo Container Scanning Technology Development*, Science Applications International Corporation, San Diego, California.

[10] D.R. Norman, J.L. Jones, B.W. Blackburn, A. Fisher, S.M. Watson, K.J. Haskell, A.W. Hunt and M. Balzer, *Radiation Safety Aspects for Pulsed Photonuclear Assessment Techniques in Outdoor Operations*, Nuclear Instruments and Methods in Physics Research Section B: Beam Interactions with Materials and Atoms. 261 (2007), pp. 913-917.

[11] R. Bentley, *Database of High-Z Signatures in Cargo*, Technologies for Homeland Security (HST), 2011 IEEE International Conference on, 2011.

[12] A. Zavadtsev, D. Zavadtsev, A. Krasnov, N. Sobenin, S. Kutsaev, D. Churanov and M. Urbant, *A Dual-Energy Linac Cargo Inspection System*, Instruments and Experimental Techniques. 54 (2011), pp. 241-248.

[13] B.R. Grogan, J.J. Henkel, J.O. Johnson, J.T. Mihalczo, T.M. Miller and B.W. Patton, *Investigation of Active Interrogation Techniques to Detect Special Nuclear Material in Maritime Environments: Boarded Search of a Cargo Container Ship*, Nuclear Instruments and Methods in Physics Research Section B: Beam Interactions with Materials and Atoms. 316 (2013), pp. 62-70.

[14] H.R. Weller, M.W. Ahmed, H. Gao, W. Tornow, Y.K. Wu, M. Gai and R. Miskimen, *Research Opportunities at the Upgraded HI Gamma S Facility RID G-2589-2011*, Progress in Particle and Nuclear Physics, Vol 62, no 1. 62 (2009), pp. 257-303.

[15] F. Albert, S.G. Anderson, D.J. Gibson, C.A. Hagmann, M.S. Johnson, M. Messerly, V. Semenov, M.Y. Shverdin, B. Rusnak, A.M. Tremaine, F.V. Hartemann, C.W. Siders, D.P. McNabb and C.P.J. Barty, *Characterization and Applications of a Tunable, Laser-Based, MeV-Class Compton-Scattering Gamma-Ray Source*, Physical Review Special Topics-Accelerators and Beams. 13 (2010), pp. 070704.

[16] S. Chen, N.D. Powers, I. Ghebregziabher, C.M. Maharjan, C. Liu, G. Golovin, S. Banerjee, J. Zhang, N. Cunningham, A. Moorti, S. Clarke, S. Pozzi and D.P. Umstadter, *MeV-Energy X Rays from Inverse Compton Scattering with Laser-Wakefield Accelerated Electrons*, Phys.Rev.Lett. 110 (2013), pp. 155003.

[17] N.D. Powers, I. Ghebregziabher, G. Golovin, C. Liu, S. Chen, S. Banerjee, J. Zhang and D.P. Umstadter, *Quasi-Monoenergetic and Tunable X-Rays from a Laser-Driven Compton Light Source*, Nature Photonics. 8 (2014), pp. 29-32.

[18] C. Liu, G. Golovin, S. Chen, J. Zhang, B. Zhao, D. Haden, S. Banerjee, J. Silano, H. Karwowski and D. Umstadter, *Generation of 9 MeV γ-Rays by all-Laser-Driven Compton Scattering with Second-Harmonic Laser Light*, Opt.Lett. 39 (2014), pp. 4132-4135.

[19] S. Banerjee, S. Chen, N. Powers, D. Haden, C. Liu, G. Golovin, J. Zhang, B. Zhao, S.D. Clarke, S. Pozzi, J. Silano, H.J. Karwowski and D. Umstadter, *Compact Source of Narrowband and Tunable X-Rays for Radiography*, Nuclear Instruments and Methods in Physics Research Section B: Beam Interactions with Materials and Atoms (2015). Available at doi:10.1016/j.nimb.2015.01.015.

[20] M.A. Flower, *Webb's Physics of Medical Imaging*, CRC Press, 2012.

[21] *10 CFR 20.1003*, US Nuclear Regulatory Commission (2009).

[22] J.I. Katz, G.S. Blanpied, K.N. Borozdin and C. Morris,*X-Radiography of Cargo Containers* , SCIENCE AND GLOBAL SECURITY. 15 (2007), pp. 49-56.

[23] J. Tümmler, R. Jung, H. Stiel, P. Nickles and W. Sandner, *High-Repetition-Rate Chirped-Pulse-Amplification Thin-Disk Laser System with Joule-Level Pulse Energy*, Opt.Lett. 34 (2009), pp. 1378-1380.

[24] C. McGuffey, A.G.R. Thomas, W. Schumaker, T. Matsuoka, V. Chvykov, F.J. Dollar, G. Kalintchenko, V. Yanovsky, A. Maksimchuk, K. Krushelnick, V.Y. Bychenkov, I.V. Glazyrin and A.V. Karpeev, *Ionization Induced Trapping in a Laser Wakefield Accelerator*, Phys.Rev.Lett. 104 (2010), pp. 025004.

[25] A. Pak, K.A. Marsh, S.F. Martins, W. Lu, W.B. Mori and C. Joshi, *Injection and Trapping of Tunnel-Ionized Electrons into Laser-Produced Wakes*, Phys.Rev.Lett. 104 (2010), pp. 025003.

[26] S.M. Khan, P.E. Nicholas and M.S. Terpilak, *Radiation Dose Equivalent to Stowaways in Vehicles*, Health Phys. 86 (2004), pp. 483-492.

[27] S. Ogorodnikov and V. Petrunin, *Processing of Interlaced Images in 4–10 MeV Dual Energy Customs System for Material Recognition*, Physical Review Special Topics-Accelerators and Beams. 5 (2002), pp. 104701.

[28] M. Gmar, E. Berthoumieux, S. Boyer, F. Carrel, D. Doré, M. Giacri, F. Lainé, B. Poumarède, D. Ridikas and A. Van Lauwe, *Detection of Nuclear Material by Photon Activation Inside Cargo Containers*, Defense and Security Symposium, 2006.

[29] H. Im and K. Song, *Applications of Prompt Gamma Ray Neutron Activation Analysis: Detection of Illicit Materials*, Applied Spectroscopy Reviews. 44 (2009), pp. 317-334.

[30] G. Zentai, *X-Ray Imaging for Homeland Security*, International Journal of Signal and Imaging Systems Engineering. 3 (2010), pp. 13-20.